IVYSPRING INTERNATIONAL PUBLISHER

Theranostics

2019; 9(5): 1288-1302. doi: 10.7150/thno.30238

Research Paper

Iron Oxide Nanoflowers @ CuS Hybrids for Cancer Tri-Therapy: Interplay of Photothermal Therapy, Magnetic Hyperthermia and Photodynamic Therapy

Alberto Curcio[1,2], Amanda K. A. Silva[2], Sonia Cabana[1,2], Ana Espinosa[2], Benoit Baptiste[3], Nicolas Menguy[3], Claire Wilhelm[2]✉ *, Ali Abou-Hassan[1]✉ *

1. Sorbonne Université, CNRS UMR 8234, Physicochimie des Electrolytes et Nanosystèmes InterfaciauX (PHENIX), 4 place Jussieu, 75005 Paris, France.
2. Laboratoire Matière et Systèmes Complexes, CNRS UMR 7057, Université Paris Diderot, 75205 Paris Cedex 13, France.
3. Sorbonne Université, MNHN, CNRS UMR 7590, IRD - Institut de Minéralogie de Physique des Matériaux et de Cosmochimie (IMPMC), 4 place Jussieu, 75005 Paris, France.

*Equal contribution

✉ Corresponding authors: ali.abou_hassan@sorbonne-universite.fr; claire.wilhelm@univ-paris-diderot.fr

Received: 2018.09.27; Accepted: 2018.12.30; Published: 2019.02.12

Abstract

Innovative synthesis routes revolutionized nanomaterial combination and design possibilities resulting in a new generation of fine-tuned nanoparticles featuring exquisite shape and constitution control. However, there is still room for improvement when it comes to the development of multi-functional nanoparticle agents merging a plurality of therapeutic functions to tackle tumors simultaneously by synergic mechanisms. Herein, we report the design of an optimized nanohybrid for cancer tri-therapy featuring a maghemite (γ-Fe2O3) nanoflower-like multicore nanoparticle conceived for efficient magnetic hyperthermia (MHT) and a spiky copper sulfide shell (IONF@CuS) with a high near-infrared (NIR) absorption coefficient suitable for photothermal (PTT) and photodynamic therapy (PDT).

Methods: Spiky-like IONF@CuS nanohybrids were obtained through a straightforward and scalable water-based template sacrificial synthesis, which allows the shell shape control by tuning polyvinylpyrrolidone (PVP) concentration. A comprehensive characterization of nanohybrid size, shape and structural properties was carried out by combining complementary TEM, SEM, HR-TEM, EELS, XRD and NTA. The all-in-one therapeutic multi-functionality was assessed on cancer cells and on tumor-bearing nude mice.

Results: Tests carried out on IONF@CuS nanohybrid aqueous dispersion demonstrated their impressive efficiency to convert light (conversion coefficient = 42 ± 6 %) and magnetic stimulation (SAR ~ 350 W g^{-1}) into heat as well as to induce concurrent reactive oxygen species (ROS) formation upon laser irradiation. Such capabilities were further confirmed in cellular environment by *in vitro* tests and at the organism level by *in vivo* tests in a murine tumor model. Notably, complete tumor regression was obtained for the PTT mode at low Cu concentration. Overall, these results allowed determining windows of applicability for each therapy individually or in combination.

Conclusions: Altogether, the obtained data evidence the successful synthesis of a unique tri-therapeutic nanoparticle featuring highly relevant assets for clinical translation such as reduced nanoparticle administered dose, reduced laser power exposure, reduced magnetic field frequency, and the possibility of serial heating cycles and therapy monitoring by photoacoustic (PA) and magnetic resonance imaging (MRI). Furthermore, the integration of the dual heating capability (MHT + PTT) with the PDT insult offers a unique asset to tackle tumors by multiple cytotoxic strategies in order to improve the therapeutic outcome in a broader spectrum of clinical conditions.

Key words: iron oxide; copper sulfide; photothermal therapy; magnetic hyperthermia; photodynamic therapy

Introduction

Research in cancer nanotherapy has experienced a remarkable expansion over the last years. Nanoparticles unique multifunctional features such as stimulus-responsiveness can overcome accuracy and efficiency limitations of current therapies and open up new avenues in the rising field of nanomedicine [1,2]. For instance, energy-absorbing nanoparticles went forward very rapidly in the implementation of hyperthermia or heat-mediated therapy [3].The assets of this therapeutic modality stem from the unique nanoparticle feature to act in the site of interest as locally confined and remotely controllable heat mediator, sparing healthy tissue by keeping its temperature at the physiological level [4]. This results in increased therapeutic efficiency and accuracy, powering a spatiotemporal controlled action while reducing invasiveness and side effects. Depending on the stimulus used as trigger, nanoparticle-mediated hyperthermia falls into two categories: magnetic hyperthermia (MHT) that exploits magnetic nanoparticles within an alternating magnetic field (AMF) [5,6], or photothermal therapy (PTT) that uses light-absorbing nanoparticles activated by near infra-red laser [7–9]. Recent trends explored the potential of merging different modalities to reach an optimized global therapeutic effect [10,11]. As such, one strategy is to combine MHT and PTT with the objective to produce a cumulative heating in the site of interest. Beyond the cumulative effect, the rationale of this combined strategy is based on the complementarity of MHT and PTT for a synergic effect. The main advantage of MHT is that it can be performed without depth limitation, which prompted magnetic hyperthermia in its way to the clinics (MagForce, Berlin) [12] to treat solid tumors. Additionally, iron oxide nanoparticles used for MHT are efficient contrast agents for MRI [13], allowing translational tracking *in vivo*. However, MHT provides a heating yield per nanoparticle amount much inferior to PTT [14,15]. At the opposite, while extremely efficient, PTT suffers from disadvantages related to limited light penetration in the tissue. Combining MHT and PTT implies providing nanomaterials with responsiveness both a magnetic field and to light in order to merge the two therapies strengths while overcoming their intrinsic limitations. As a result, important advantages, which are quite relevant from a clinical standpoint, may be achieved: (i) reduced nanoparticle administered dose; (ii) reduced laser power exposure; (iii) reduced current intensity; (iv) single injection of an all-in-one nanoparticle. In addition, multi-responsive nanomaterials are image-trackable, by photo-acoustic imaging for the light-absorbing part, or by magnetic resonance imaging (MRI) for the magnetic part. The proposed strategy for elaborating such magneto-plasmonic hybrids with vocation to combine MHT with PTT, is to provide a magnetic unit optimized for MHT (size, structure, magnetization), and a plasmonic one tailored for PTT (NIR absorption). In order to reach high-temperature levels in MHT, many magnetic particles [16] have been designed to provide the best nanoheaters over the last decade, including magnetic nanocubes [17,18], nanoflower-like multi-cores [19], core-shells [20,21] or magnetosomes [22,23]. For the first NIR (NIR-I) biological window, gold-based engineered nanoparticles such as nanorods [24], nanostars [25,26] or nanoshells [27], have shown the best heating capacities due to enhanced absorption. Thus, although still in their infancy, optimized magneto-plasmonic hybrids combining MHT and PTT have merged the best performing MHT and PTT nano-heaters [11]. Magnetic nanocubes and magnetic nanoflowers with gold shells were indeed successfully assembled to demonstrate the concept of a magneto-photo-thermal modality strategy [28–31]. Of note, several studies implicating magneto-plasmonic hybrids for other applications, including multimodal imaging [32], SERS [31,33], PA imaging [34], are far more numerous. Recently, semiconductor and plasmonic nanoparticles such as sub-stoichiometric copper sulfide compounds ($Cu_{2-x}S$ denoted as CuS in the following) have emerged as concurrent candidates for efficient PTT, as well as for photo-acoustic imaging with deep penetration [35,36].Compared to available gold nanoparticles with dimensions suitable for biomedical applications, CuS semiconductor nanomaterials exhibit fine-tuned localized surface plasmon resonance (LSPR) and large extinction coefficients in the second NIR (NIR-II) biological window where the imaging resolution (signal-to-noise ratio) is optimal and light has its maximum depth of penetration in tissues due to the reductions in the intensity of autofluorescence and the absorption/scattering of photons [37]. Such optical properties can be tailored through molecular or self-assembly bottom-up chemical approaches [29,38,39]. Moreover, copper sulfide is biodegradable and its synthesis cost is much cheaper than gold (1 mol of CuS is 330$, while 1 mol of Au costs 52k$) [40], which is an important criterion for economically-viable manufacturing, clinical translation and long-term applications. Last but not least, CuS also offers the possibility to integrate different therapies like radio-photo therapy [41,42] thanks to radioactive cation exchange [43], and reactive oxygen species (ROS) production [44] giving the opportunity to combine PTT and photodynamic therapy (PDT) in one single material without the need for further addition of photosensitizer molecules,

which are prone to photo-bleaching and photo-degradation. PDT is based on the combined action of three components: a photosensitizer, light, and oxygen. Upon irradiation at an appropriate wavelength, the photosensitizer is activated and transfers its excited-state energy to surrounding oxygen. This results in the production of ROS, such as singlet oxygen, which will induce cell death [45,46]. CuS photodynamic properties are particularly interesting considering the demonstrated synergism between PDT and PTT: increased blood flow leads to more O_2 available [47], while ROS weaken the heat-shock cellular defense [48]. As such, multiple nanomaterials have been proposed to combine PDT with PTT, mostly associating photosensitizers with gold-based nanoparticles [49,50]. Only a few studies have also successfully combined PDT with MHT, using, for instance, photosensitizers-labeled magnetic liposomes [51,52] or photosensitizer-loaded magnetic nanoemulsions [53]. Although still very limited, multifunctional inorganic Fe_2O_3@CuS core−shell nanocomposites synthesis has been described for biomedical applications: Tian *et al* [54] reported a thermal decomposition synthesis method in which spherical-shaped Fe_3O_4 nanocrystals were encapsulated into $Cu_{2-x}S$ thin shells forming ultrathin (<10 nm) Fe_3O_4@CuS core−shell nanocomposites for dual-modal imaging and PTT; more recently Wu *et al* [55] described a room temperature synthesis method in which truncated octahedron 27-nm CTAB-coated Fe_3O_4 nanoparticles were modified with copper oxide as a sacrificial template for the formation of copper sulfide after a sulfidation step. The obtained rattle-type Fe_3O_4@CuS nanostructures were used to conduct magnetically guided photo-induced hyperthermia at first and second NIR biological windows. So far, the magnetic component was used only to endow the compounds with magnetic targeting or MRI contrast, and the use of copper sulfide shell was only limited to PTT. To the best of our knowledge neither the design of a nanocomposite combining iron oxide and copper sulfide with optimized properties for MHT and PTT has been reported, nor the evaluation of the three modalities *i.e.* MHT, PTT, and PDT together and their possible synergistic properties, which potentially stem from the combination of the different materials, has been ever explored.

Herein, we report the successful synthesis of a core@shell theranostic nanohybrid composed of a nanoflower-like iron oxide multicore structure, optimized for MHT application, and a copper sulfide shell with enhanced absorption properties for PTT and PDT applications. Remarkably, tuning polyvinyl-pyrrolidone (PVP) concentration during the synthesis allowed reaching an unprecedented spiky flower-like copper sulfide shell around the single magnetic nanoflower. Such nanohybrid allowed exploring the concept of a tri-therapeutic strategy merging MHT, PTT and PDT using iron oxide@CuS core-shell. The multiple expected functions of such hybrids at increasing degrees of complexity from test tubes to animals were assessed, with the aim to describe a critical comparison with the stand-alone treatments (MHT and PTT), and to provide effective windows of applicability.

Methods

Materials

All reagents were of analytical purity and used without further purification. Iron(II) chloride tetra-hydrate ($FeCl_2 \cdot 4H_2O$, 99%), sodium hydroxide (NaOH, 99.99%), diethylene glycol (DEG, 99%), N-methyldiethanolamine (NMDEA, 99%), nitric acid (HNO_3, 70%), copper(II) nitrate hemi(pentahydrate) ($Cu(NO_3)_2 \cdot 2.5H_2O$ ≥99.99%), polyvinylpyrrolidone (PVP, Mw 55 kDa), hydrazine hydrate (55%), ammonium sulfide solution ($(NH_4)_2S$, 20%), dihydrorhodamine 123 (DHR123 ≥95%), sodium cacodylatetrihydrate (≥98%), glutaraldehyde solution (25% in H_2O), hydrogen peroxide solution (30 wt. % in H_2O) and formalin solution (10%) were purchased from Sigma-Aldrich (France). Iron(III) chloride hexahydrate ($FeCl_3 \cdot 6H_2O$, 99%) and ethanol were obtained from VWR (France). Alamar Blue™ cell viability reagent was purchased from Thermo-Fisher.

Instrument

Electron transmission images were obtained by 120 kV TEM FEI-Tecnai 12. UV-Vis-NIR characterization was performed with the real-time Avaspec-USB2 spectrometer. Zeta potential analysis was performed on NanoZS and nanoparticle tracking analysis was performed by Nanosight LM10 (Malvern). Microplate reading was obtained by EnSpire reader (PerkinElmer). NPs concentration was determined by elemental analysis using ICP-OES (Thermo Scientific). Energy filtered elemental mapping and high-resolution TEM analysis were performed by 200 kV FE (Field Emission) analytical electron microscope JEM-2100F (JEOL). The X-ray powder diffraction (XRD) patterns were recorded using an X'Pert Pro Panalytical diffractometer equipped with a Co *Ka* radiation source (λ_{Ka1} = 1.78901 Å, λ_{Ka2} = 1.79290 Å) with an X'Celerator detector. SEM imaging was performed by Zeiss Supra 40 VP Scanning Electron Microscope (5 kV). Emission spectra of fluorescent molecules were measured by a Cary Eclipse fluorescence spectrophotometer. To measure the temperature increase of solutions and tumors the IR thermal camera FLIR SC7000 (FLIR Systems) was

used. Alternating magnetic field (AMF) was applied by DM3-H magnetic hyperthermia device (Nanoscale Biomagnetics). Photothermal therapy was obtained using a1064 nm CW laser diode coupled to an optic fiber (Laser Components S.A.S) with an adjustable power up to 5 W.

Synthesis of water-soluble iron oxide nanoflowers (IONFs)

In brief, in a 3 neck flask 1.082 g (4 mmol) of $FeCl_3 \cdot 6H_2O$ and 0.398 g (2 mmol) of $FeCl_2 \cdot 4H_2O$ were completely dissolved in 80 g of a liquid mixture of DEG and NMDEA with 1:1 (v/v) ratio and the solution was stirred for 1 h. Separately, 0.64 g (16 mmol) of NaOH was dissolved in 40 g of polyols and mixed to the iron chlorides solution for another 3 h. Then, the solution was heated with a linear ramp up to 220 °C in 50 min using a heating mantle. Once the temperature reached 220 °C, the solution was stirred for 2.5 h and then cooled slowly to room temperature. The black sediments were separated magnetically and washed with a mixture of ethanol and ethyl acetate (1:1, v/v) several times to eliminate organic and inorganic impurities. A treatment with 10% nitric acid at 80 °C for 45 min was performed to remove possible iron hydroxides and to achieve a complete oxidation of the nanoparticles. Next the particles were washed twice with acetone and diethyl ether and redispersed in water.

Synthesis of the Copper Sulfide Shell

The IONF@CuS nanohybrids were synthesized in a 2 step reaction through a template sacrificial synthesis method. In the first step, Cu_2O shell was formed on the magnetic core as follow: 100 µL of IONF dispersion (95 mM of Fe), corresponding to 0.5 mg of Fe, were diluted in 30 mL of milliQ H_2O and mixed with different amounts of PVP 55kDa from 0.15 to 0.9 g. The resulting mixture was shaken vigorously (orbital shaker at 500 RPM) for 15 min before the addition of 10 mg of cupric nitrate $Cu(NO_3)_2$. The solution was shaken again for 15 min. The pH of the solution was adjusted to 4 by adding nitric acid (0.15 M). Next, 8 µL of hydrazine 55% (diluted with H_2O up to 100 µL) were rapidly injected in the solution leading to a cloudy straw yellow colored dispersion, which was allowed to mix for 3 more min (pH ~ 5.6). The core-shell IONF@Cu_2O nanoparticles were washed twice with milliQ H_2O by centrifugation (8100 g for 60 min) and stored at 4 °C or immediately used for the following step.

The second step of the reaction consisted in the sulfidation of the Cu_2O shell of the nanohybrids synthesized previously. After diluting the sample in 30 mL of milliQ H_2O, 22 µL of ammonium sulfide $S(NH_4)_2$ 21% solution were added and the reaction was kept at room temperature for 1 h under vigorous shaking and the green-brown resulting suspension was washed twice with by centrifugation (8100 g for 10 min) with milliQ H_2O and stored at 4 °C.

Morphology and Optical Characterization

Transmission electron microscopy (TEM), UV-vis-NIR spectrometry, dynamic light scattering (DLS), nanoparticle tracking analysis (NTA), high-resolution TEM (HR-TEM), electron energy loss spectroscopy (EELS), X-ray diffraction (XRD) analysis were used to characterize the samples at the different steps of their synthesis.

Heating measurements in solution

Analysis of the heating profiles of the solution was obtained placing 100 µL of IONF@CuS aqueous dispersion in a 0.5 mL tube at the concentration of 20, 40, 80, 160 and 320 mM of Cu (correspondent to 3.1, 6.2, 12.5, 25 and 50 mM of Fe, respectively) in the middle of the coils of the magnetic hyperthermia device and simultaneously to 4 cm distance from the laser source. The samples were irradiated with the alternating magnetic field (AMF) at 471 kHz of frequency and 18 mT of field, or with 1064 nm laser at the power of 0.3 W cm^{-2} and a spot size of 1 cm^2 or both at the same time. The increase in temperature was measured by a FLIR SC7000 infrared thermal imaging camera.

The SAR, defined as the power dissipation per unit mass of iron (W g^{-1}), was calculated as follows:

$$SAR = \frac{C\,V}{m}\frac{\mathrm{d}T}{\mathrm{d}t}$$

where m is the total mass of iron in the sample, $C$is the specific heat capacity of the sample (C_{water} = 4185 J L^{-1} K^{-1}), V is the sample volume (300 µL), and $\mathrm{d}T/\mathrm{d}t$ is the temperature increase at the initial linear slope (~ 30 s). The concentration in iron in all the samples was set approximately to 2 g L^{-1}.

The photothermal conversion coefficient η of the IONF@CuS was calculated as follows:

$$\eta = \frac{hA(T_{Max} - T_{Amb}) - Q_{Dis}}{I_0 \cdot S\,(1 - 10^{-A_{1064}})}$$

Where h is the heat transfer coefficient, A is the area of the container, $T_{Max} - T_{Amb}$ is the temperature change, Q_{Dis} represents heat dissipated from light absorbed by the quartz sample cell itself and the solvent, I_0 is incident laser power in W, S is the illuminated area in cm^2 and A_{1064} is the absorbance at the IONF@CuS at 1064 nm. The coefficient was calculated for 6 different Cu concentrations from 0.2 to 20 mM.

Reactive oxygen species (ROS) in solution and in cell determination

ROS levels revelation was carried out using the dihydrorhodamine 123 (DHR), a non-fluorescent ROS indicator that exhibits green fluorescence once oxidized. Nanohybrids dispersions at different concentrations were mixed with a solution of the DHR at 1.5 µM in water in order to obtain Cu and Fe concentration ranging from 0.025 to 2.4 mM of Cu and from 4 to 375 µM of Fe, correspondingly. The fluorescence of the probe increased with time and also in presence of the nanohybrids leading to an augmentation of the probe signal. Such increase was proportional to the nanohybrids concentration. Thus, in order to evaluate the effect of the laser on ROS generation in presence of the IONF@CuS, a non-laser irradiated control solution was simultaneously analyzed at the same hybrids concentration. The ratios of the laser-induced fluorescence signal over the control one were plotted, together with the laser only control value. To exclude the heat component responsible to the ROS induction, the condition at the highest nanohybrids concentration (2.4 mM of Cu and 375 µM of Fe) was heated to the same temperature (54 °C and ΔT = 21 °C) that was reached by the laser-treated corresponding sample.

Since the reduced DHR probe is non-toxic and neutral, it can passively diffuse across the cell membranes, where if oxidized it becomes cationic and unable to go out from the cell, therefore it acts as direct *in situ* indication of ROS production in cells. ROS levels were analyzed in PC3 cells previously incubated with IONF@CuS at 1.6 mM of Cu and 250 µM of Fe for 4 h. After the incubation, the cells were rinsed several times with PBS 1x and incubated with a solution of DHR 10 µM in PBS 1x for 5 min at 37 °C. Then the probe solution was discarded and the cells were rinsed several times with PBS 1x before adding complete DMEM media without phenol red. After 10 min of equilibration in the incubator at 37 °C, the cells were analyzed by confocal microscopy before and after illumination with the 1064 nm laser for 15 min at 6 W cm^{-2}. As control, a sample treated in the same way but without nanohybrids was also analyzed before and after laser irradiation. The superoxide radical ($\bullet O_2^-$) formation was shown using the specific probe 1,3-diphenylisobenzofuran (DPBF), a fluorescent dye that progressively decrease its emission at 477 nm in presence of increasing concentration of the superoxide anion. The probe was used at a concentration of 15 µM in H_2O with and without the adding of IONF@CuS (130 mM of Cu and 20 mM of Fe). The 500 µL solutions were exposed to the 1064-nm laser for 5 min at 1 W cm^{-2}, in the same conditions and for the same time, before being simultaneously analyzed and normalized with the non-irradiated solutions. The probe sensitivity to the heating (at the same temperature reached by nanohybrids + laser) and the hydrogen peroxide have been showed as negative controls.

Cell culture, uptake and biocompatibility and cytotoxicity assay

Human prostate adenocarcinoma PC3 cells (ATCC® CRL-1435™, France) were cultured in Dulbecco's Modified Eagle's Medium (DMEM, high glucose) supplemented with 10% Fetal Bovine Serum (heat-inactivated FBS) and 1% Penicillin-Streptomycin (5000 U/mL) under 37 °C, 5% CO_2 and 95% relative humidity.

For the uptake and the biocompatibility assays, 5 × 10^5 cells per well were seeded and allowed to grow until near confluence in 24 multi-well culture plates prior to incubation with nanohybrids. IONF@CuS at the concentration of 0.1, 0.4 and 1.6 mM of Cu, corresponding to 15, 62 and 250 µM of Fe, were dissolved in cell media and incubated with cells for 1, 4 and 16 h. At the end of the incubation, the cells were thoroughly washed 3 times with PBS 1x and incubated for an additional 2 h with complete DMEM medium to remove any non-internalized nanohybrids before further analysis.

To assess the degree of uptake, the iron load associated with single cells was quantified by single cell magnetophoresis. After the incubation, the cells were trypsinized to obtain a dilute suspension. The magnetophoretic mobility of cells towards a magnet creating a magnetic field B of 150 mT and a uniform field gradient (grad B) of 17 T m^{-1} was recorded by video microscopy. Under these conditions, the magnetic driving force acting on cells (M × grad B, where M is the cell magnetic moment) is balanced by the viscous force ($3 \pi \eta d v$, where η is the medium viscosity, d is the cell diameter and v is the cell velocity). The cell magnetization was thus deduced from the velocity and diameter of each cell. The velocity and diameter of 100 cells were measured, yielding to the distribution of iron load per cell population.

To assess the IONF@CuS biocompatibility, PC3 metabolic activity was measured using a resazurin based test (Alamar Blue™). After washing steps, cells were incubated with resazurin containing non-supplemented DMEM without phenol red, according to manufacturer instructions. Then, the medium was transferred in 96 well plates and the fluorescence due to the reduction of resazurin (oxidized form) to resorufin by cell activity was quantified with a microplate reader (excitation 570 nm, emission 585 nm). The results were normalized

respect untreated controls in the same conditions. All measurements were performed in quadruplicate.

For the MHT and PTT cytotoxic therapeutic analysis, 10^6 PC3 cells were seeded in T25 culture flasks and 24 h later they were incubated with 0.04, 0.16, 0.32 and 1.6 mM of Cu, corresponding to 6.2, 25, 50 and 250 µM of Fe dissolved in complete DMEM (or with only complete medium for the CTRL) for 16 h. At the end of the incubation, the cells were thoroughly washed 3 times with PBS 1x, trypsinized, pelleted and 5×10^6 cells were resuspended in 50 µL complete DMEM without phenol red inside a 0.5 mL tube. The tube was placed inside a thermostated sample holder which temperature was kept constant at physiological conditions (37 °C) by circulating water into the circuit (see Figure S5). MHT (471 kHz and 18 mT for 30 min) or PTT (1064 nm laser at 0.1 or 0.3 W cm^{-2} for 5 min) were applied while the temperature increase was monitored by the IR camera. At the end of the treatment, the cells were diluted in complete DMEM, seeded in 24 multi-well culture plates at a density of 5×10^5 cells per well and allowed to adhere overnight. Then their metabolic activity was evaluated as described above.

In vivo experiments

All animal experiments were carried out according to the relevant European standards. 30 pathogen-free 9-week-old immunodeficient athymic nude NMRI female mice (Janvier Laboratories, France) were acclimatized for 1 week (Animalerie Buffon, Institute Jacques Monod, Paris). PC3 cells (2×10^6 in 100 µL isotonic saline) were injected in the right and left flanks to induce solid tumors. The tumor volume has been calculated following the formula:

$$V = \text{length} \times \text{width} \times \text{height} \times \pi/6$$

The treatments were performed 4 to 7 weeks after the injection, when the tumors had reached a volume ≥ 0.125 cm^3 and the mice weighed ~ 30 g. The animals were divided into 8 groups: nanohybrids injected + PTT (at 0.6, 3 and 15 mM of Cu); nanohybrids injected + MHT (at 650 mM of Cu); controls (without laser, laser only and nanohybrids injected at 15 mM and 650 mM of Cu without any treatment). The IONF@CuS suspension (50 µL) was intratumorally injected into the xenograft at different concentrations as described above and one single treatment was carried out 1 h following the injection. For PTT and for the control laser only, mice were anesthetized with isoflurane, and then the tumor was illuminated with 1064 nm laser at 1 W cm^{-2} for 10 min. For MHT, mice were anesthetized with intraperitoneal injection of a mixture of ketamine and xylazine, and then the tumor was treated with AMF at the frequency of 471 kHz and the field of 18 mT. During the treatment, the heating was recorded with an infrared thermal imaging camera. The animals were sacrificed 12 days after the treatment and in any case before the tumors reached 1.5 cm^3. For histological analysis, mice were sacrificed 24 h after the treatment and their tumors were fixed in 10% formalin solution in PBS overnight, before paraffin inclusion and cutting. 4 µm thick slices were treated with hematoxylin/eosin/saffron (HES), Masson, Pearls and Rodanine stainings and then analyzed by optical microscopy. For electron microscopy analysis the excised tumors were divided into 1 mm^3 pieces and fixed for 2 h with 2% glutaraldehyde in 0.1 M cacodylate buffer. Then the sample processing was performed with a microwave tissue processor for electron microscopy. The steps included contrasted with Oolong Tea Extract (OTE) 0.5% in 0.1 M Na cacodylate buffer, post-fixed with 1% osmium tetroxide containing 1.5% potassium cyanoferrate, gradually dehydrated in ethanol (30% to 100%) and gradually embedded in epoxy resins. Ultrathin slices (70 nm) were collected onto 200 mesh coppergrids and counterstained with lead citrate prior to being observed with a Hitachi HT 7700 TEM operated at 80 kV (Elexience – France).

Statistical analysis

All values are reported as means and standard error of the mean. Significant differences were determined using a Tukey's test in one-way analysis of variance (ANOVA). * denotes for p-value < 0.05 (significant result), ** for p-value < 0.01 (very significant), and *** for p-value < 0.001 (highly significant).

Results and Discussion

Nanohybrids production: from core to shell.

The choice for the magnetic core took into account the need for a nanomaterial with optimized properties for magnetic hyperthermia application. Therefore, the criteria relied on a high specific absorption rate (SAR), an indicator of thermal dissipation per gram of magnetic material, and thus of its heating capacity. Moreover, the selected nanomaterial should show resistance and colloidal stability to withstand the subsequent steps of the hybrid synthesis. Iron oxide nanoflowers (IONFs) were chosen as magnetic cores for the nanohybrids because of their high SAR values, in the 1000 W g^{-1} range [19], and because, they are completely superparamagnetic and do not tend to form dipole-dipole chains and aggregates that could hinder their heating efficiency [56], unlike other efficient but

strongly interacting nanoheaters [57]. Therefore, IONFs successfully meet the starting requirements. They were synthesized by hydrolysis of the iron(II) and iron(III) precursors in a polyol mixture, following a reported procedure [19] (see experimental section for further details). IONFs are multicore maghemite monocrystalline nanoparticles constituted by the assembly of small grains of approximately 11 nm, which forms a flower-shaped structure. Figure 1A shows a TEM image of water dispersed IONFs featuring a mean diameter of 25.5 ± 2.7 nm. To cover them with a copper sulfide shell two synthesis steps were used [55]. The first step consisted in the formation of a sacrificial template by reducing copper ions through successive addition of hydrazine on IONFs previously modified with PVP in water. Immediately after hydrazine addition, the suspension became slightly cloudy featuring an intense straw yellow color indicating the formation of IONF@Cu_2O nanohybrids. In this step, PVP is used as a scaffold for the physical absorption of the Cu_2O nuclei (resulting from copper reduction) around the IONF core, directing the assembly of Cu_2O shell [58]. The core-shell IONF@Cu_2O intermediate was then transformed, during the second step, in IONF@CuS by replacing the oxygen ions with sulfur ions in a Kirkendall reaction [59] (see experimental section for more details). The successful formation of the intermediate IONF@Cu_2O and the final IONF@CuS nanostructure was confirmed by TEM (Figure 1B-D) and UV-Vis-NIR absorption spectroscopy (Figure 1E). The particle size increased from 25.5 nm (IONF core) to 100 ± 10 nm after the addition of hydrazine due to the formation of the Cu_2O nanoparticles isotropic assembly around the iron oxide core (Figure 1B). The UV-Vis-NIR of the IONF@Cu_2O nanohybrids demonstrated a strong absorption peak at 454 nm in accordance with the yellow color observed after the addition of hydrazine. During the sulfidation step of the IONF@Cu_2O hybrids, the solution underwent color change with time from yellow to deep green. Such change can be clearly seen by UV-Vis-NIR that showed the disappearance of the band at 450 nm and the appearance of a large LSPR band in the NIR-II region indicating the transformation of Cu_2O into plasmonic CuS shell by Kirkendall effect. TEM observations at the end of this step revealed structural modification and reorganization of the Cu_2O shell producing hollow CuS architectures, as already reported [55]. Remarkably, we found also that the shape/organization and the optical properties of the resulting IONF@CuS nanohybrids could be tuned by varying the initial PVP concentration used as a scaffold for the nucleation of the Cu_2O shell impacting the final shape of the CuS during the sulfidation step. As shown by TEM, when the sulfidation step was done on IONF@Cu_2O nanohybrids produced in high PVP concentration (30 g L^{-1}), the resulting nanohybrids (TEM diameter = 126 ± 4.8 nm) presented an isotropic hollow copper sulfide shell with a blunt surface (Figure 1C). Such rattle-type morphology has been reported recently by Wu *et al* [55]. Conversely, for a lower concentration of PVP (5 g L^{-1}), the shell of the resulting IONF@CuS nanohybrids indicated a spiky flower-like morphology with an average diameter by TEM of 120.4 ± 7.3 nm formed by the assembly of anisotropic shape nanoparticles (Figure 1D). As both synthesis conditions lead to similar shape and size of the intermediate nanohybrid IONF@Cu_2O, we may attribute such difference to the fact that increased amount of PVP produces different packing of the sacrificial Cu_2O nanoparticles, leading to different resistance and diffusion paths of sulfur in the intermediate nanostructure during the Kirkendall process consequently resulting in the formation of different morphologies. The optical properties of the blunt and spiky nanohybrids recorded at the same copper concentration (1 mM) using UV-Vis-NIR absorption spectroscopy are shown in Figure 1E. The LSPR band centered on 1050 nm for both nanohybrids can be clearly observed evidencing their plasmonic properties. Moreover, a higher absorption intensity of the spiky flower-like nanostructures compared to the blunt ones could be evidenced. Such differences can be attributed to disparities in the size, the anisotropy, the composition of the nanoparticles *i.e.* building blocks forming the ultimate nanohybrids as well as the final geometry of the core@shell structures [29,38]. Considering that our prime interest in this work is to achieve tri-therapy with optimized magnetic and optical properties to allow deeper tissue penetration and efficient heating, the unprecedented spiky flower-like IONF@$Cu_{2-x}S$ nanohybrids were chosen as the best candidates. Their morphology, as well as their physical properties, were further investigated and studied hereafter. Figure 2A illustrates the HR-TEM image of one single IONF@$Cu_{2-x}S$ nanohybrid showing the presence of isolated IONF in the core of a hollow structure surrounded by a shell (from 40 to 60 nm) formed by the assembly of copper sulfide spiky nanostructures. To reveal the 3D ultrastructure and morphology of the assembled nanohybrids, we conducted scanning electron microscopy (SEM) (Figure 2B). It evidenced that the spiky flower-like morphology of the shell observed by TEM results from the assembly of copper sulfide nanoflakes with a thickness of ~ 3-5 nm having different orientations. Ultrafine copper sulfide nanoparticles such as the ultrathin nanoflakes have received an increasing attention recently as they can

produce intense LSPR because of their enhanced number of superficial defects [60]. HR-TEM magnified section of the core (Figure 2C) of the nanohybrid confirmed the presence of the iron oxide lattice, as also reported by the corresponding fast Fourier transform (FFT) (Figure 2D) characteristic of a monocrystalline structure which has been indexed with a spinel *Fd-;m* cubic phase with a lattice parameter a = 8.396 Å relative to maghemite (JCPDS 00-039-1346) in accordance with the results from XRD (Figure S1).The structure analysis of the copper sulfide shell by HR-TEM image at higher magnification and its FFT pattern were also obtained (Figure 2E-F). Interplanar distances deduced from FFT pattern are compatible with the sub-stoichiometric djurleite (JCPDS01-071-1383). These results are in accordance with the chemical analysis obtained by inductively coupled plasma atomic emission spectroscopy (ICP-AES), where a Cu/S ratio ~ 1.9 was determined but also with XRD where djurleite could be indexed, even though covellite (JCPDS 00-006-0464) could be also observed in the final samples. Identification of copper chalcogenide crystallographic phases using XRD is particularly difficult since they exist in a wide variety of compositions and crystal structures [61]. We also used energy-filtered TEM (EFTEM) for assessing the structure of these nanohybrids. Figure 2H-K shows composition mapping for IONF@CuS NPs. A higher density of copper and sulfur elements was observed at the periphery than at the center, and iron elements were distributed internally. These observations indicated that the IONFs were enclosed in the hollow copper sulfide shell.

IONF@CuS: a bi-modal nanoheater efficient for both MHT and PTT.

Suspensions of IONF@CuS spiky nanohybrids (from now on IONF@CuS) were chosen for further evaluation due to their improved absorption properties compared to the blunt ones. Their hydrodynamic diameter in water was measured by nanoparticle tracking analysis (NTA, Figure S2), prior to their use revealing a mean hydrodynamic size of 156 nm. Their surface charge measured by zeta potential in water at pH 7 was −14.1 mV precluding inter-particle interactions and preventing their aggregation while supporting a good stability in water. IONF@CuS heating efficiency was then evaluated using either magnetic or photo-stimulation in order to study MHT or the PTT modalities individually, or both at the same time. Measurements started at room temperature and continued up to reaching a steady state temperature (typically within 5 min). Typical IR images are shown in Figure 3, after 5 min exposure to alternating magnetic field (Figure 3A), laser (Figure 3B), or both (Figure 3C). For all cases, the heating was measured at different nanohybrids concentrations, in the range of iron concentrations of 3-50 mM, and equivalent copper concentrations of 20-320 mM. During MHT modality, nanohybrids were exposed to a magnetic field at a frequency of 471 kHz and a field of 18 mT, which is close to the safe domain of application of magnetic field (limit set at H × f = 5 × 10^9 A m^{-1} s^{-1}, here H × f = 6.7 × 10^9 A m^{-1} s^{-1}). Figure 3A clearly shows that the temperature elevation increases linearly with the concentration. As a result, the SAR is independent of the concentration, with SAR value reaching ~ 350 W g^{-1}. The SAR was also measured for the bare magnetic IONF core, which featured a SAR of ~ 500 W g^{-1} in the same conditions. Such a value is among the highest values reported for the frequency/ field used (471 kHz of frequency and 18 mT of field) [19,62,63]. As a comparison, the magnetic nanocubes, which are admitted to be between the most efficient MHT agents, have a SAR value of 550 W g^{-1} relative to 320 kHz of frequency and 18 mT of

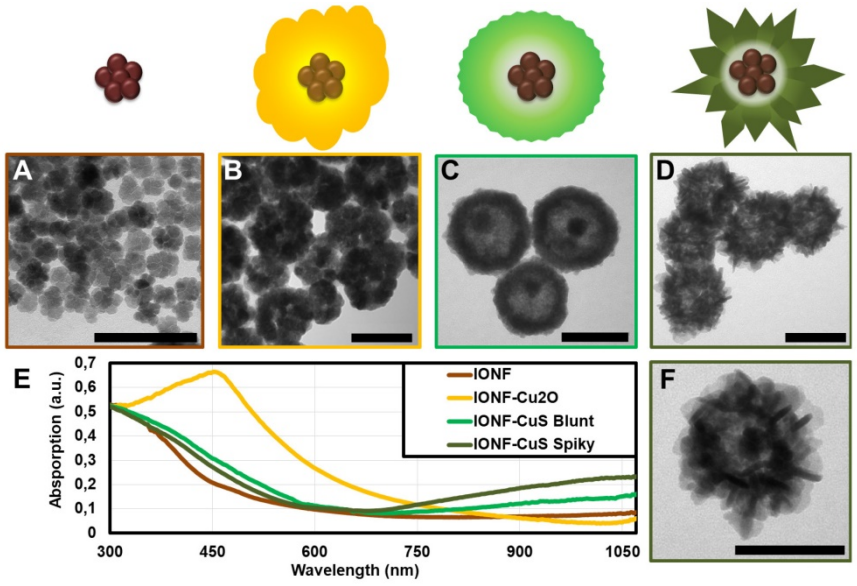

Figure 1. Electronic transmission microscopy images of the synthesis products (A) IONFs, (B) IONF@Cu_2O, (C) IONF@CuS blunt and (D) IONF@CuS spiky flower-like as well as their corresponding schematic sketches; (f) Image at higher magnification of a single IONF@CuS spiky; (E) UV-Vis-NIR spectra of the IONF (brown), IONF@Cu_2O (yellow), IONF@CuS blunt (light green) and IONF@CuS spiky flower-like (dark green). Both the IONF@CuS samples were at the same concentration of 1 mM Cu. Scale bar = 100 nm.

field intensity [18]. The decreased SAR value of the core@shell nanohybrid is attributed to the increase in its diameter that affects the Brownian relaxation time. Notably, we ruled out any impact the CuS coating may have on the magnetic properties of the iron oxide core (see Figure S3 for the magnetization curve of the IONF core only, or of the IONF@CuS hybrid, unchanged).

PTT experiments (Figure 3B) were carried out using a 1064 nm laser and the power density was set to 0.3 W cm^{-2} by positioning the fiber tip at a 4 cm distance from the target, which resulted in a spot size of 1 cm^2. The photothermal conversion efficiency at this wavelength was calculated using the method used by Roper *et al* [28] resulting in the value of 42% ± 6. This very high efficiency puts these nanohybrids among the most promising materials for PTT. In contrast with MHT, during PTT the heating performance tends to saturate when increasing the nanohybrid concentration, as already reported [14]. This saturation phenomenon can be explained by looking at the light-to-heat energy transfer equation:

$$I_0 \cdot S(1 - 10^{-A}) \cdot \eta = m_{\text{sample}} \cdot C \cdot \mathrm{d}T/\mathrm{d}t$$

where I_0 is the incident laser power in W, S is the illuminated area in cm^2, A is the absorbance of the sample at the irradiation wavelength, η is the photothermal conversion efficiency from laser energy to thermal energy, m_{sample} is the sample mass (in this case of the water) in g, C denotes the specific heat capacity (C_{water} = 4 × 18 J g^{-1} K^{-1}), and $\mathrm{d}T/\mathrm{d}t$ denotes the initial slope of the temperature increase. Consequently, at high concentration, 10^{-A} becomes negligible, and the initial heating $\mathrm{d}T/\mathrm{d}t$ remains almost constant with increasing concentrations. As a result, while the heating at high nanohybrids doses was similar for MHT and PTT, heating generation efficiency at low doses is much higher for PTT. For instance, only a few degrees of heating was achieved at 40 mM of Cu (equivalent to 6.2 mM of Fe) for MHT, which is quite insignificant when compared to an increase of 14 °C reached for the PTT modality at the same concentration. However, at higher concentration (e.g. [Cu] = 320 mM; [Fe] = 50 mM), heating with MHT is equivalent with photo-heating (about 30 °C). We designed a specific thermostated support to apply simultaneously AMF and Laser (see Figure S4 for details). This dual mode (Figure 3C) then allowed providing a cumulative effect at the full concentration range tested. Indeed, the heating obtained by bi-modal stimulation closely corresponded to the sum of the heating obtained for every single modality. These data prove the versatility of nanohybrids and attest to the cumulative effect of the two heating approaches, promising for the delivery of therapeutic heating to cancer tissues. Of note, the stability of the nanohybrids was conserved after several heating cycles (Figure S5). As a result, the heating efficiency was constant for repeated application, and the colloidal stability was retained. This is an important point considering that light-responsive nanoparticles, such as gold nanorods, may undergo degradation during repeated heating cycles [64].

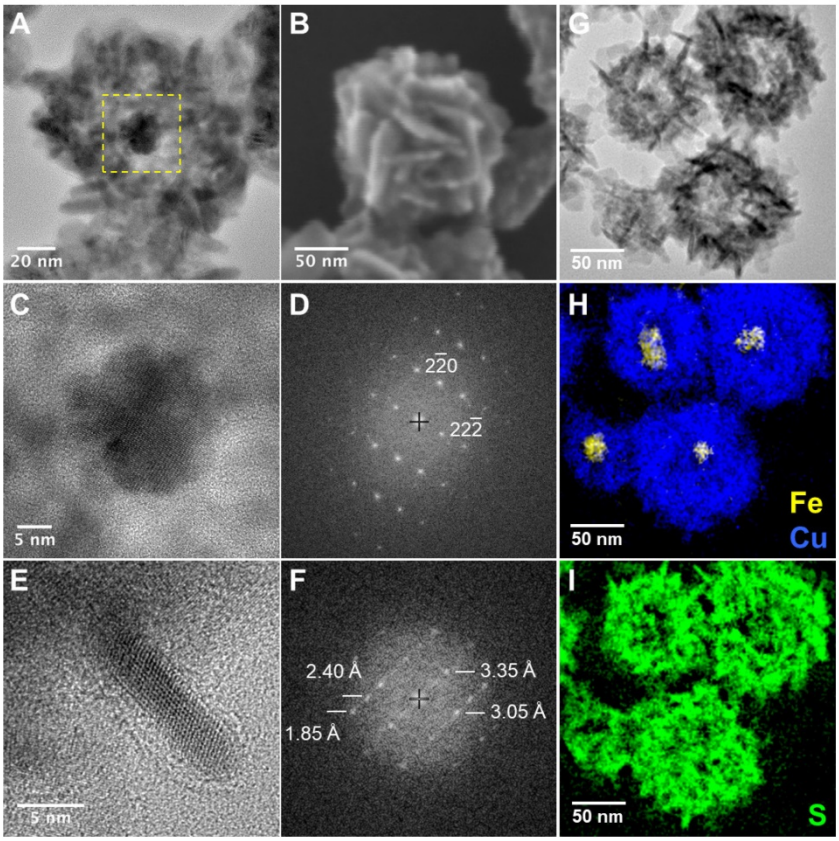

Figure 2. (A) HR-TEM image showing the hollow core@shell nanostructure of a single spiky flower-like IONF@CuS nanohybrid, yellow dashed square corresponds to the image (C); (B) SEM image of the same nanostructure revealing the organization of CuS nanoflakes; (C) HR-TEM image of the magnetic core of the IONF@CuS showing the nanoflower shape and (D) corresponding indexed FFT; (E) HR-TEM image of one flake of the CuS shell and (F) corresponding FFT in which interplanar distances are given with uncertainties equal to 0.05 Å. Interplanar distances in djurleite: d_{800} = 3.362 Å, d_{442} = 3.039 Å, d_{842} = 2.394 Å, d_{1242} = 1.873 Å; EFTEM elemental mapping of the flower-like spiky IONF@CuS (G-I): zero loss peak TEM bright field image (G) and related EFTEM elemental images recorded at respectively Fe-L2,3 and Cu-L2,3 edges (H) and S-L2,3 edge (I).

Photo-driven ROS formation by IONF@CuS: a third functional asset.

CuS has recently been reported to induce ROS formation [65,66], rendering it eligible to mediate PDT, a third therapeutic cytotoxic function. We thus tested IONF@CuS nanohybrids for the production of ROS and, in particular, if this could be enhanced by IR laser irradiation. In order to focus on the laser impact on ROS generation, these experiments were carried out in more diluted Cu concentration range to avoid any ROS signal saturation, and with a higher laser power of 1 W cm^{-2}. As shown in Figure 3D, the ROS amount detected by the fluorescent signal of the ROS detection probe dihydrorhodamine 123 (DHR) after the laser exposition (and normalized by the ROS formation without laser at the same concentration and incubation time) increases linearly with the copper concentration. Accordingly, the temperature increased linearly with Cu concentration in the investigated range, as expected, leading to a maximum ΔT of 21 °C (corresponding to a final T of 46 °C). To rule out the possible impact of heating itself on the ROS induction, a control suspension was heated at the same temperature of 46 °C in a water bath for the same time length. The ROS increase at 2.4 mM of Cu and 46 °C is about 10 times less for the water bath condition when compared to the laser-induced heating. ROS generation by CuS have been attributed by others to the leakage from the nanostructure of Cu(I) under reducing conditions such as in presence of ascorbic acid or glutathione, which can undergo Haber-Weiss reactions resulting in the formation of radicals [65,67]. Intriguingly, our solutions did not contain any reducing agent and the heating capacity of the nanostructures was maintained after several cycles even for high copper concentrations (Figure S5), which indicates clearly that copper leakage is negligible and the reaction is probably occurring within the nanostructure. Moreover, the observed behavior in ROS generation at constant DHR probe concentration and increasing Cu, *i.e.* linear dependency at low Cu concentrations and saturation at high Cu concentrations, demonstrates clearly a catalytic behavior of the CuS. Haber-Weiss reaction was proposed by other groups as a plausible mechanism for ROS generation [65]. In order to investigate the possible occurrence of such mechanism we measured specifically the superoxide radical ($\bullet O_2^-$) using the probe 1,3-diphenylisobenzofuran (DPBF). Results in Figure S6 showed that the nanohybrids trigger the generation of the superoxide radicals in absence or presence of laser, yet with a two-fold increase under laser application. In absence of the laser the Cu(I) of the nanohybrids can catalyze the formation of the superoxide from molecular oxygen, as already reported [68]. Then the superoxide anions can undergo dismutation leading to hydrogen peroxide formation and generation of hydroxyl radicals through a Cu(I) catalyzed Fenton process. This mechanism allows to explain why the nanohybrids form ROS even in absence of a laser. Moreover, the incubation of the magnetic nanoflowers (at similar Fe concentration and incubation time than used with the hybrids) with the DHR probe, with or without laser did not show any increase in the fluorescence, confirming the unique role of Cu in the generation of ROS. Thus, herein we propose that the CuS can act as a catalyst for ROS via superoxide anion ($\bullet O_2^-$) generation and the NIR laser seems to act in synergy to ROS production by speeding-up the kinetics of the Haber-Weiss reaction resulting in the formation of more ROS.

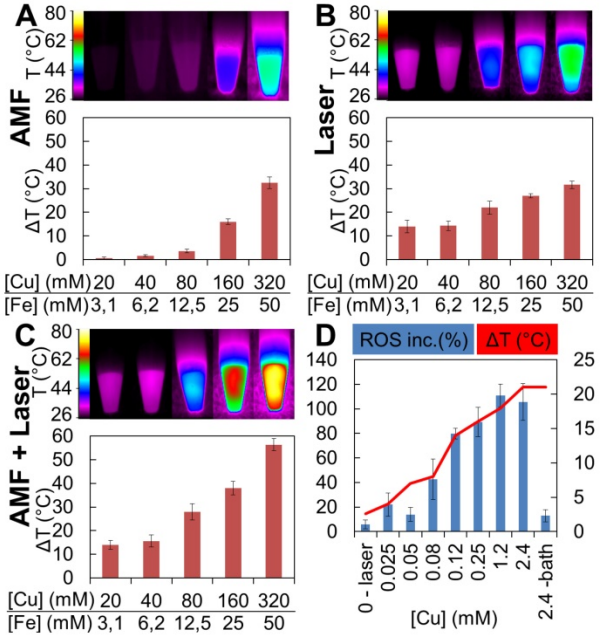

Figure 3. Heating profiles obtained by MHT, PTT and bimodal stimulation. Temperature increase was registered for 100 µL of IONF@CuS nanohybrids dispersion at different concentration (20, 40, 80, 160, 320 mM of Cu and 3.1, 6.2, 12.5, 25, 50 mM of Fe, respectively) exposed to (A) alternating magnetic field (AMF) at 471 kHz and 18 mT, (B) 1064 nm laser at the power of 0.3 W cm^{-2} and (C) the combination of both modalities. In the top panel, typical infrared images after 5 min heating are displayed. (D) ROS production in nanohybrid dispersions following laser stimulation: the blue columns display the relative ROS increase as a function of Cu concentration after 5 min laser exposure (1064 nm at 1 W cm^{-2}) while the red curve shows the temperature elevation obtained by the nanohybrid dispersions (500 µL). Relative ROS increase was normalized by the signal obtained from the non-irradiated samples. The ROS level was detected by the probe added to the nanohybrids at a concentration of 1.65 mM that provides a fluorescent signal when oxidized by ROS. As a control, the nanohybrids were heated at the same temperature reached by the highest concentration using a water bath for the same duration.

Magnetic and photo-induced cytotoxicity *in vitro*: comparative therapeutic efficiencies.

First, we measured the cellular uptake of the IONF@CuS nanohybrids by single-cell magnetophor-

esis, providing a measure of the amount of superparamagnetic iron internalized within each cell (Figure 4A). For the concentration of nanohybrids dispersed in the cell medium of 1.6 mM of Cu, corresponding to 0.25 mM of Fe, during 16 h incubation with PC3 cells, ~ 11 pg of Fe per cell was internalized. By contrast, the reduction of the nanohybrids concentration by 4 times results in less than half internalization decrease, while shortening the incubation time of 4 times leads to one-fourth of nanoparticle uptake in both nanoparticle concentration scenarios. This indicates a probable saturation of the cell uptake machinery when shifting IONF@CuS nanohybrids concentration to the highest dose levels. The uptake ratio normalized by the amount given per cell is 4.3%, 13.7% and 56.5% for the lower concentration, 2.1%, 7.1% and 23.7% for the higher concentration for 1, 4 and 16 h of incubation, respectively. These data were confirmed by ICP analysis where a 61% Cu uptake was found after 16 h incubation at the concentration of 0.4 mM of Cu. In parallel, intrinsic cytotoxicity of the IONF@CuS nanohybrids was measured on PC3 cancer cell line after incubation with nanohybrids dispersed in the cell medium for 3 time lengths (1, 4 and 16 h) at 3 different concentrations (0.1, 0.4 and 1.6 mM of Cu – 6.3, 25 and 100 ppm of Cu) and without any heating modality. After 24 h from the beginning of the nanohybrids incubation, no impact on cell metabolic activity was observed, indicating that nanohybrids do not induce by themselves an important cytotoxic effect (Figure 4B). Next, we determined the cytotoxic therapeutic efficiency of the MHT and PTT, as shown in Figure 4C, using again the metabolic assay. PC3 cells were incubated 16 h with different concentration of nanohybrids ([Cu] from 0.04 to 1.6 mM), before being collected and pelleted to perform MHT or PTT. One can estimate the Fe content in the 50 µL cellular sample (containing 5 × 10^6 cells) from the data of magnetophoresis, providing the average of 6.5 and 11 pg of Fe per cell (relative to the two highest incubation concentrations), which corresponds to the concentration of the cell sample of about 12 and 20 mM of Fe (equivalent to 75 and 130 mM of Cu). Remarkably, the respective heating increments (ΔT = 20 and 27 °C) overlap well with the values found in solution (see Figure 3B, for [Cu] = 80 and 160 mM, with ΔT = 22 and 28 °C, respectively). PTT was very efficient to induce cell death even at the lower concentrations as the temperature rapidly reached up to 45 and 57 °C for 0.04 and 0.16 mM of Cu, respectively. In the latter condition, nearly total cell death (90%) is achieved within 5 min of PTT (blue lines and blue columns). On the other hand, MHT only induced a very small heating effect (from 37 °C to ~ 40 °C; ΔT = 3 °C) corresponding to a slight decrease of cell viability (15%) even at the highest dose level. This important discrepancy between MHT and PTT therapeutic efficiencies highlights the superior performance of PTT as long as the target depth enables laser reaching. We next tested if combining both MHT and PTT in a single modality could still be a therapeutic asset, even if MHT as stand-alone therapy appears much less efficient than PTT. Indeed, Figure 4D shows that at lower laser density (0.1 W cm^{-2} that mimics the situation in deep tumors where laser penetration is strongly decreased) the simultaneous application of AMF and laser improves by 20% the therapeutic efficiency for both the conditions tested (see Dual), in a statistically significant way. Finally, it is also important to emphasize here is that the laser power used (0.3 W cm^{-2}) is quite low with respect to the ones generally reported in the literature [69]. Such an impressive efficiency at low laser power is probably due to the combined effects of both the PTT and the PDT. In order to investigate if PDT is indeed occurring within cells, we used the DHR probe to detect the intracellular ROS production by IONF@CuS nanohybrids within doped PC3 cells (incubation with 1.6 mM of Cu for 4 h). As shown in Figure 4D, the presence alone of the IONF@CuS induces the increase of ROS signal (bottom-left box) without the laser irradiation. However, the signal becomes more intense and localized in the subcellular compartments (endosomes, lysosomes) after the IR laser exposure for 15 min. The laser-treated control (top-right box) shows no increase of ROS signal in the absence of IONF@CuS nanohybrids. These data suggest that the IONF@CuS nanohybrids can mediate the photodynamic process that induces ROS-triggered cytotoxic insult, this process being boosted upon NIR light stimulation.

In vivo tumor therapy: MHT versus PTT/PDT.

To confirm the therapeutic potential of the IONF@CuS nanohybrids, they were injected at different concentrations in PC3 xenograft-bearing nude mice (50 µL injected in tumors ≤ 0.125 cm^3). Figure 5A shows typical echographic and photoacoustic images of the tumor before and after injection. As it could be expected, these data demonstrate the feasibility of image-guided nanohybrid therapy by PA imaging thanks to their excellent absorption in the IR. Figure 5B shows TEM image of the tumors 24 h after injection, displaying the intratumoral integrity of the nanohybrids, and their subsequent internalization within tumor cells. Figure 5C provides a panel of IR images illustrating the temperature reached after 10 min (for PTT) or 30 min

(for MHT) application. The average temperatures are shown in Figure 5D. The temperature increase is particularly important under laser stimulation, reaching 53 °C for injected concentrations as small as 0.6 mM of Cu and 0.1 mM of Fe. By contrast, to provide a measurable temperature increase of 4 °C using the magnetic field, it was necessary to increase the concentration of a thousand-fold up to 650 mM of Cu (corresponding to 100 mM of Fe). Interestingly, increasing the dose injected in the tumor higher than 3 mM of Cu lead to no significant increase in the heat produced during laser application, again confirming the absorption saturation and in turn that the PTT has a greater efficiency at low doses, as already noticed [14]. Tumor growth was then monitored over 13 days after treatment. Figure 5E illustrates the relative tumor growth for all conditions, and Figure S7 shows representative photographs of tumor-bearing mice 13 days after treatment. As expected, all three conditions of photo-treatment (0.6, 3, and 15 mM of Cu) led to an almost total tumor regression, slightly less marked for the 0.6 mM condition. Very interestingly, the MHT condition at high dose (650 mM Cu MHT) provided a comparable treatment efficacy than this low laser dose. This was slightly unexpected considering the small temperature increase. However, it is probably the reflection of the total penetration of the magnetic field within the tumor and of the mechanical stress triggered at the lysosome sites, as recently reported for MHT [70]. It is worth mentioning that such a high dose also triggers *per se* a small but detectable cytotoxicity (tumor growth of control condition with 650 mM of Cu in Figure 5C is impacted without treatment). By contrast, for the 15 mM Cu CTRL condition, the impact of injection on the tumor growth is low, similar to the effect of the laser only, and not significant. All therapeutic effects were confirmed by histological stainings (Figure 5F) performed 24 h after the end of the treatments: in detail, the HES staining shows severe and diffused necrosis in the sample treated with PTT at 15 mM of Cu (15 PPT) and also important toxicity for the MHT treated sample injected with 650 mM of Cu (650 MHT) while no inflammation was found its corresponding control (650 Ctrl). Masson trichrome colorations denote also a strong collagen denaturation for both the PTT and MHT treated samples while the tumors injected at the high nanoparticle dose but not treated show no difference with control. The massive presence of IONF@CuS injected in both high doses (650 Ctrl and 650 MHT), especially in the cortical part of the tumor, was pointed out by the Pearls and Rodanine stainings, highlighting the iron and the copper deposit, respectively. By contrast, in the tumors injected with 15 mM of Cu and treated by PTT (15 PTT) the iron and copper signals were very light, nevertheless the huge therapeutic impact.

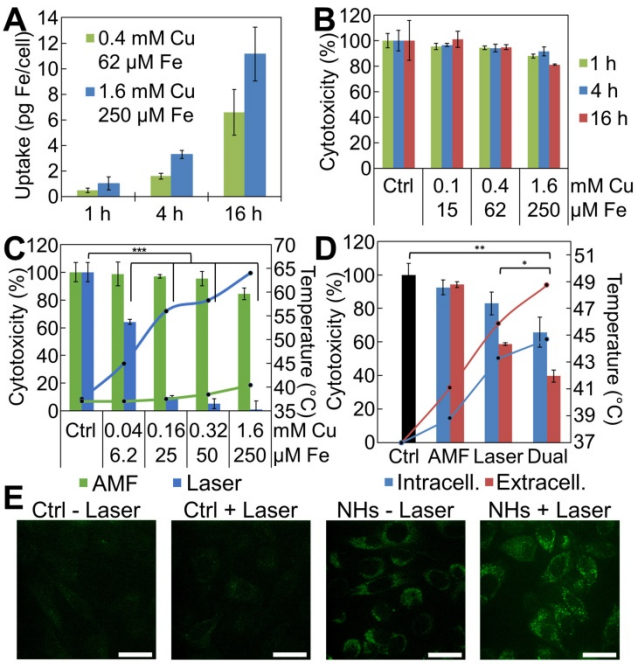

Figure 4. IONF@CuS nanohybrids uptake and cytotoxicity *in vitro* on PC3 cell line: (A) Cellular iron uptake per single cell, quantified by single cell magnetophoresis, reflects the amount of IONF@CuS internalized after 1, 4 and 16 h of incubation at 2 different concentrations. (B) Metabolic activity of PC3 cells at different concentrations of IONF@CuS nanohybrids following 1, 4 or 16 h of incubation. The Alamar Blue analysis, performed 24 h after the beginning of the incubation, shows negligible cytotoxicity even at the highest nanohybrid concentration used. (C) Composed plot illustrating the cell treatment study: depending from the modality used (green for AMF, 470 kHz – 18 mT and blue for 1064 nm laser, 0.3 W/cm²) and the nanohybrid concentrations during incubation, the heating (lines in the plot) varies (starting from 37 °C), and it correlates with the effect on the viability (bars in the plot). Herein the treatments have been performed on 5 × 10⁶ cells resuspended in 50 µL. The indicated concentrations correspond to the nanohybrids in the incubation media; (D) Evaluation of tri-therapy efficiency by comparing stand-alone MHT and laser-mediated therapies (PTT + PDT), with the dual application of AMF (470 kHz – 18 mT) and laser (0.1 W cm^{-2}). Very low laser power was used to mimic situation in deep tumors, which strongly decreases laser penetration, but not MHT performance. PC3 cancer cells samples were prepared by incubating overnight the nanohybrids at [Cu] = 0.32 mM (intracellular condition, blue) and preparing a cells pellet in 50 µL, or by injecting directly within the same tumor-like cell mass the nanohybrids at a final concentration of [Cu] = 80 mM ([Fe] = 12.5 mM) (extracellular condition, red). The temperature (starting from 37 °C) is plotted as lines (secondary axis), and the cytotoxicity as bars (primary axis). Significance between groups was determined using one-way analysis of variance (ANOVA), with Tukey's test (* $p < 0.05$, ** $p < 0.01$, *** $p < 0.001$); (E) ROS detection in PC3 cells by confocal microscopy: after the incubation with IONF@CuS nanohybrids (NHs) (1.6 mM of Cu and 250 µM of Fe for 4 h) the fluorescent DHR signal already is present (bottom-left box) and it increases even more after the laser exposure (1064 nm laser at 6 W cm^{-2} for 15 min). Scale bar = 100 µm.

Conclusions

The successful synthesis of nanohybrids combining a nanoflower-like core optimized for magnetic hyperthermia and a CuS spiky shell honed for IR-triggered PTT and PDT allows providing a class of all-in-one nanohybrids merging MHT, PTT and PDT in a tri-therapeutic strategy. MHT and PTT were successfully combined to provide a cumulative

heating enabling reduced doses to be used. Furthermore, the integration of this dual heating capability to a photodynamic insult is a unique asset to tackle tumors by distinct cytotoxic strategies so that cancer cells may be eliminated more efficiently, and ultimately improving the therapeutic outcome in a broader spectrum of clinical conditions. Besides a cumulative effect, the cytotoxic mechanisms of each strategy may enhance each other, leading to a much-sought synergism. In this paper, we demonstrated that the three therapeutic modalities are functional both *in vitro* and *in vivo*, all using a single nanohybrid. However, the PTT modality appears far more efficient than the MHT counterpart. If the tumor location is not deep in the body being easily accessible to laser exposure, phototherapy will be the preferred option to trigger a compelling therapeutic effect. However, even if MHT requires higher nanohybrid doses obtaining a temperature increase limited to only a few degrees, this functionality is of high interest in case of deeply entangled tumors where laser penetration is partly impaired. Last but not least, the magnetic core provides the hybrids with MRI detection, allowing an in-depth imaging complementary to the photoacoustic one. In overall, IONF@CuS hybrids provide a multi-faceted theranostic tool that may find its place in the next-generation approaches for image-guided synergic tumor therapy.

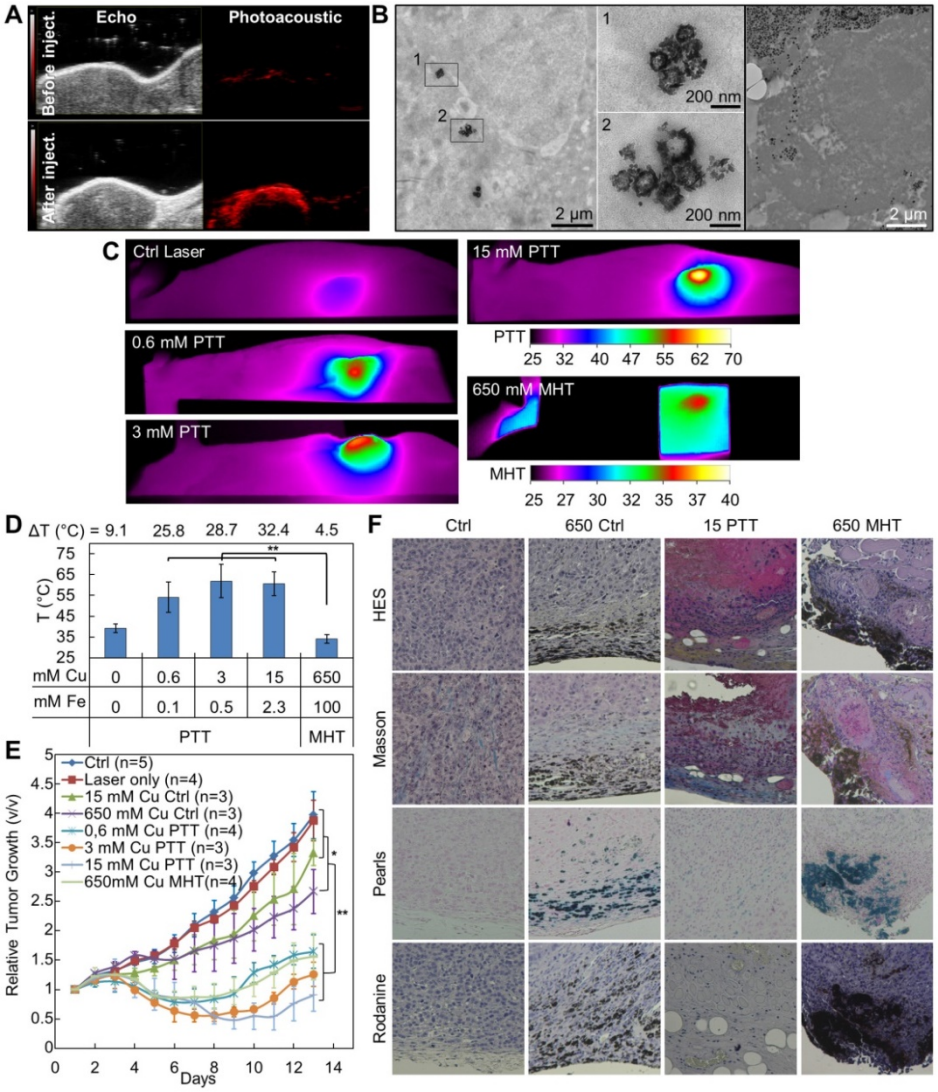

Figure 5. *In vivo* treatment characterization: (A) Ultrasound and corresponding photoacoustic images (λ = 950 nm) of a xenograph tumor before and after intratumoral injection of 50 µL of IONF@CuS nanohybrids dispersion at 75 mM of Cu and 12 mM of Fe; (B) TEM micrographs showing the nanohybrid in the tumor tissue after 24 h from the injection and their intra- and extracellular distribution; (C) Representative infrared thermal images after 10 min treatment (1064 nm laser at 1 W cm^{-2}) of tumor not injected (Ctrl Laser) or injected with nanohybrids at the concentration of 0.6, 3 or 15 mM of Cu (0.6-, 3- and 15 mM PTT) or after 30 min treatment (471 kHz and 18 mT) of tumor injected with nanohybrids at a concentration of 650 mM of Cu (650 mM MHT); (D) The corresponding average temperatures at the end of the treatments; (E) Average tumor growths at the conditions corresponding to the temperature analysis (Figure 5D) plus the untreated control, during the 13 days following the treatment. Significance between groups was determined using one-way analysis of variance (ANOVA), with Tukey's test (** $p<0.01$, * $p<0.05$); (F) Histology sections of tumor 24 h after the treatment stained with hematoxylin/eosin/saffron (HES) for viable/inflamed tissue, Masson for collagen fibers, Pearls for iron deposits and Rodanine for copper deposits in non-injected tumors (Ctrl) and injected with IONF@CuS at 650 mM of Cu not treated (650 Ctrl), at 15 mM of Cu + PTT (15 PTT) and 650 mM of Cu + MHT (650 MHT).

Abbreviations

AC: alternate current; AMF: alternating magnetic field; CTAB: cetrimonium bromide; CuS: copper sulfide; DHR: dihydrorhodamine 123; DMEM: Dulbecco's Modified Eagle's Medium; DPBF: 1,3-diphenylisobenzofuran; EELS: electron energy loss spectroscopy; EFTEM: energy-filtered TEM; FBS: fetal bovine serum; FFT: fast Fourier transform; HES: hematoxylin-eosin-saffron; HR-TEM: high resolution TEM; ICP-AES: inductively coupled plasma atomic emission spectroscopy; IONF: iron oxide nanoflower; LSPR: localized surface plasmon resonance; MHT: magnetic hyperthermia; MRI: magnetic resonance imaging; NIR: near-infrared; NTA: nanoparticle tracking analysis; OTE: Oolong Tea Extract; PA: photoacoustic imaging; PBS: phosphate-buffered saline; PDT: photodynamic therapy; PTT: photothermal therapy; PVP: polyvinylpyrrolidone; ROS: reactive oxygen species; SAR: specific absorption rate; SEM: scanning electron microscopy; SERS: surface-enhanced Raman spectroscopy; TEM: transmission electron microscopy; UV-Vis: ultraviolet-visible; XRD: X-ray diffractions.

Supplementary Material

Supplementary figures and tables.
http://www.thno.org/v09p1288s1.pdf

Acknowledgments

We acknowledge technical support from Cochin HistIM Facility (histology), Christine Péchoux from INRA in Jouy-en-Josas for TEM preparation and analysis, the staff of the animal housing facility at the Jacques Monod Institute for animal experiments, Prof. Mihaela Delcea and Dr. Mykola Medvidov from ZIK HIKE, University of Greifswald for SEM imaging.

Funding

We thank the City Hall of Paris in the frame of the Research in Paris program 2015 (MagPlas-CANCER project), Sorbonne University & Paris Diderot University, the CNRS and the DIM Nano-K Ile-de-France (3TPhy project) for financial support.

Contributions

CW and AAH contributed equally.

Competing Interests

The authors have declared that no competing interest exists.

References

1. Zhang P, Hu C, Ran W, Meng J, Yin Q, Li Y. Recent progress in light-triggered nanotheranostics for cancer treatment. Theranostics. 2016; 6: 948-68.
2. Tayo LL. Stimuli-responsive nanocarriers for intracellular delivery. Biophys Rev. 2017; 9: 931-40.
3. Beik J, Abed Z, Ghoreishi FS, Hosseini-Nami S, Mehrzadi S, Shakeri-Zadeh A, et al. Nanotechnology in hyperthermia cancer therapy: from fundamental principles to advanced applications. J Control Release. 2016; 235: 205-21.
4. Jaque D, Martínez Maestro L, Del Rosal B, Haro-Gonzalez P, Benayas A, Plaza JL, et al. Nanoparticles for photothermal therapies. Nanoscale. 2014; 6: 9494-530.
5. Vallejo-Fernandez G, Whear O, Roca AG, Hussain S, Timmis J, Patel V, et al. Mechanisms of hyperthermia in magnetic nanoparticles. J Phys D: App Phys. 2013; 46: 312001.
6. Rosensweig RE. Heating magnetic fluid with alternating magnetic field. J Magn Magn Mater. 2002; 252: 370–374.
7. Opoku-Damoah Y, Wang R, Zhou J, Ding Y. Versatile nanosystem-based cancer theranostics: design inspiration and predetermined routing. Theranostics 2016; 6: 986–1003.
8. Lal S, Clare SE, Halas NJ. Nanoshell-enabled photothermal cancer therapy: impending clinical impact. Acc Chem Res. 2008; 41: 1842-51.
9. Lamanna G, Battigelli A, Ménard-Moyon C, Bianco A. Multifunctionalized carbon nanotubes as advanced multimodal nanomaterials for biomedical applications. Nanotech Rev. 2012; 1: 17-29.
10. Yan H, Shang W, Sun X, Zhao L, Wang J, Xiong Z, et al. "All-in-one" nanoparticles for trimodality imaging-guided intracellular photo-magnetic hyperthermia therapy under intravenous administration. Adv Funct Mater. 2018; 28: 1705710.
11. Espinosa A, Bugnet M, Radtke G, Neveu S, Botton GA, Wilhelm C, et al. Can magneto-plasmonic nanohybrids efficiently combine photothermia with magnetic hyperthermia? Nanoscale. 2015; 7: 18872-7.
12. Jordan A, Scholz R, Maier-Hauff K, Johannsen M, Wust P, Nadobny J, et al. Presentation of a new magnetic field therapy system for the treatment of human solid tumors with magnetic fluid hyperthermia. J Magn Magn Mater. 2001; 225: 118-26.
13. Hu F, MacRenaris KW, EA Waters, Schultz-Sikma EA, Eckermann AL, Meade TJ. Highly dispersible, superparamagnetic magnetite nanoflowers for magnetic resonance imaging. Chem Commun. 2010; 46: 73-5.
14. Espinosa A, Kolosnjaj-Tabi J, Abou-Hassan A, Plan Sangnier A, Curcio A, Silva AKA, et al. Magnetic (hyper)thermia or photothermia? Progressive comparison of iron oxide and gold nanoparticles heating in water, in cells, and in vivo. Adv Funct Mater. 2018; 28: 1803660.
15. Saeed M, Ren W, Wu A. Therapeutic applications of iron oxide based nanoparticles in cancer: basic concepts and recent advances. Biomat Sci. 2018; 6: 708-25.
16. Xie W, Guo Z, Gao F, Gao Q, Wang D, Liaw BS, et al. Shape-, size- and structure-controlled synthesis and biocompatibility of iron oxide nanoparticles for magnetic theranostics. Theranostics. 2018; 8: 3284-307.
17. Martinez-Boubeta C, Simeonidis K, Makridis A, Angelakeris M, Iglesias O, Guardia P, et al. Learning from nature to improve the heat generation of iron-oxide nanoparticles for magnetic hyperthermia applications. Sci Rep. 2013; 3: 1652.
18. Guardia P, Di Corato R, Lartigue L, Wilhelm C, Espinosa A, Garcia-Hernandez M, et al. Water-soluble iron oxide nanocubes with high values of specific absorption rate for cancer cell hyperthermia treatment. ACS Nano. 2012; 6: 3080-91.
19. Hugounenq P, Levy M, Alloyeau D, Lartigue L, Dubois E, Cabuil V, et al. Iron oxide monocrystalline nanoflowers for highly efficient magnetic hyperthermia. J. Phys Chem C. 2012; 116: 15702-12.
20. Mandal S, Chaudhuri K. Magnetic core-shell nanoparticles for biomedical applications. In: Sharma SK, Ed. Complex magnetic nanostructures. 1st ed. New York: Springer International Publishing; 2017, 425–453.
21. Ortega D, Vélez-Fort E, García DA, García R, Litrán R, Barrera-Solano C, et al. Size and surface effects in the magnetic properties of maghemite and magnetite coated nanoparticles. Philos Trans A Math Phys Eng Sci. 2010; 368: 4407-18.
22. Plan Sangnier A, Preveral S, Curcio A, A KAS, Lefevre CT, Pignol D, et al. Targeted thermal therapy with genetically engineered magnetite magnetosomes@RGD: photothermia is far more efficient than magnetic hyperthermia. J Control Release. 2018; 279: 271-81.
23. Céspedes E, Byrne JM, Farrow N, Moise S, Coker VS, Bencsik M, et al. Bacterially synthesized ferrite nanoparticles for magnetic hyperthermia applications. Nanoscale. 2014; 6: 12958-70.
24. Freddi S, Sironi L, D'Antuono R, Morone D, Donà A, Cabrini E, et al. A molecular thermometer for nanoparticles for optical hyperthermia. Nano Lett. 2013; 13: 2004-2010
25. Espinosa A, Silva AK, Sanchez-Iglesias A, Grzelczak M, Pechoux C, Desboeufs K, et al. Cancer cell internalization of gold nanostars impacts their photothermal efficiency in vitro and in vivo: toward a plasmonic thermal fingerprint in tumoral environment. Adv Healthc Mater. 2016; 5: 1040-8.
26. Senthil Kumar P, Pastoriza-Santos I, Rodriguez-Gonzalez B, Javier Garcia de Abajo F, Liz-Marzan LM. High-yield synthesis and optical response of gold nanostars. Nanotechnology. 2008; 19: 015606.
27. Ayala-Orozco C, Urban C, Bishnoi S, Urban A, Charron H, Mitchell T, et al. Sub-100nm gold nanomatryoshkas improve photo-thermal therapy efficacy in large and highly aggressive triple negative breast tumors. J Control Release. 2014; 191: 90-7.
28. Roper DK, Ahn W, Hoepfner M. Microscale heat transfer transduced by surface plasmon resonant gold nanoparticles. J Phys Chem C. 2007; 111: 3636-41.

29. Liu M, Xue X, Ghosh C, Liu X, Liu Y, Furlani EP, et al. Room-temperature synthesis of covellite nanoplatelets with broadly tunable localized surface plasmon resonance. Chem Mater. 2015; 27: 2584-90.
30. Kim J, Park S, Lee JE, Jin SM, Lee JH, Lee IS, et al. Designed fabrication of multifunctional magnetic gold nanoshells and their application to magnetic resonance imaging and photothermal therapy. Angew Chem Int Ed Engl. 2006; 45: 7754-8.
31. Huang J, Guo M, Ke H, Zong C, Ren B, Liu G, et al. Rational design and synthesis of gamma Fe_2O_3@Au magnetic gold nanoflowers for efficient cancer theranostics. Adv Mater. 2015; 27: 5049-56.
32. Reguera J, Jimenez de Aberasturi D, Henriksen-Lacey M, Langer J, Espinosa A, Szczupak B, et al. Janus plasmonic-magnetic gold-iron oxide nanoparticles as contrast agents for multimodal imaging. Nanoscale. 2017; 9: 9467-80.
33. Quaresma P, Osório I, Dória G, Carvalho PA, Pereira A, Langer J, et al. Star-shaped magnetite@gold nanoparticles for protein magnetic separation and SERS detection. RSC Adv. 2014; 4: 3659-67.
34. Wu CH, Cook J, Emelianov S, Sokolov K. Multimodal magneto-plasmonic nanoclusters for biomedical applications. Adv Funct Mater. 2014; 24: 6862-71.
35. Ku G, Zhou M, Song S, Huang Q, Hazle J, Li C. Copper sulfide nanoparticles as a new class of photoacoustic contrast agent for deep tissue imaging at 1064 nm. ACS Nano. 2012; 6: 7489-96.
36. Yang K, Zhu L, Nie L, Sun X, Cheng L, Wu C, et al. Visualization of protease activity in vivo using an activatable photo-acoustic imaging probe based on CuS nanoparticles. Theranostics. 2014; 4: 134-41.
37. Antaris AL, Chen H, Cheng K, Sun Y, Hong G, Qu C, et al. A small-molecule dye for NIR-II imaging. Nat Mater. 2016; 15: 235-42.
38. Xie Y, Carbone L, Nobile C, Grillo V, D'Agostino S, Della Sala F, et al. Metallic-like stoichiometric copper sulfide nanocrystals: phase- and shape-selective synthesis, near-infrared surface plasmon resonance properties, and their modeling. ACS Nano. 2013; 7: 7352-69.
39. Bu X, Zhou D, Li J, Zhang X, Zhang K, Zhang H, et al. Copper sulfide self-assembly architectures with improved photothermal performance. Langmuir. 2014; 30: 1416-23.
40. Li Y, Lu W, Huang Q, Huang M, Li C, Chen W. Copper sulfide nanoparticles for photothermal ablation of tumor cells. Nanomedicine. 2010; 5: 1161-71.
41. Yi X, Yang K, Liang C, Zhong X, Ning P, Song G, et al. Imaging-guided combined photothermal and radiotherapy to treat subcutaneous and metastatic tumors using iodine-131-doped copper sulfide nanoparticles. Adv Funct Mater. 2015; 25: 4689-99.
42. Zhou M, Zhao J, Tian M, Song S, Zhang R, Gupta S, et al. Radio-photothermal therapy mediated by a single compartment nanoplatform depletes tumor initiating cells and reduces lung metastasis in the orthotopic 4T1 breast tumor model. Nanoscale. 2015; 7: 19438-47.
43. Riedinger A, Avellini T, Curcio A, Asti M, Xie Y, Tu R, et al. Post-Synthesis Incorporation of ^{64}Cu in CuS Nanocrystals to Radiolabel Photothermal Probes: A Feasible Approach for Clinics. J Am Chem Soc. 2015; 137: 15145-51.
44. Angele-Martinez C, Nguyen KV, Ameer FS, Anker JN, Brumaghim JL. Reactive oxygen species generation by copper(II) oxide nanoparticles determined by DNA damage assays and EPR spectroscopy. Nanotoxicology. 2017; 11: 278-88.
45. Allison RR, Sibata CH. Oncologic photodynamic therapy photosensitizers: a clinical review. Photodiagnosis Photodyn Ther. 2010; 7: 61-75.
46. Robertson CA, Evans DH, Abrahamse H. Photodynamic therapy (PDT): a short review on cellular mechanisms and cancer research applications for PDT. J Photochem Photobiol. 2009; 96: 1-8.
47. Yanase S, Nomura J, Matsumura Y, Nagata T, Fujii T, Tagawa T. Synergistic interaction of 5-aminolevulinic acid-based photodynamic therapy with simultaneous hyperthermia in an osteosarcoma tumor model. Int J Oncol. 2006; 29: 365-73.
48. Frank J, Lambert C, Biesalski HK, Thews O, Vaupel P, Kelleher DK. Intensified oxidative and nitrosative stress following combined ALA-based photodynamic therapy and local hyperthermia in rat tumors. Int J Cancer. 2003; 107: 941-8.
49. Xing R, Liu K, Jiao T, Zhang N, Ma K, Zhang R, et al. An injectable self-assembling collagen-gold hybrid hydrogel for combinatorial antitumor photothermal/photodynamic therapy. Adv Mater. 2016; 28: 3669-76.
50. Yu X, Bi J, Yang G, Tao H, Yang S. Synergistic effect induced high photothermal performance of Au Nanorod@Cu_7S_4 yolk–shell nanooctahedron particles. J Phys Chem C. 2016; 120: 24533-41.
51. Di Corato R, Béalle G, Kolosnjaj-Tabi J, Espinosa A, Clément O, Silva AKA, et al. Combining magnetic hyperthermia and photodynamic therapy for tumor ablation with photoresponsive magnetic liposomes. ACS Nano. 2015; 9: 2904-16.
52. Bolfarini GC, Siqueira-Moura MP, Demets GJF, Morais PC, Tedesco AC. In vitro evaluation of combined hyperthermia and photodynamic effects using magnetoliposomes loaded with cucurbit[7]uril zinc phthalocyanine complex on melanoma. J Photochem Photobiol. 2012; 115: 1-4.
53. De Paula LB, Primo FL, Pinto MR, Morais PC, Tedesco AC. Evaluation of a chloroaluminium phthalocyanine-loaded magnetic nanoemulsion as a drug delivery device to treat glioblastoma using hyperthermia and photodynamic therapy. RSC Adv. 2017; 7: 9115-22.
54. Tian Q, Hu J, Zhu Y, Zou R, Chen Z, Yang S, et al. Sub-10 nm Fe_3O_4@$Cu_{2-x}S$ core-shell nanoparticles for dual-modal imaging and photothermal therapy. J Am Chem Soc. 2013; 135: 8571-7.
55. Wu Z-C, Li W-P, Luo C-H, Su C-H, Yeh C-S. Rattle-type Fe_3O_4@CuS developed to conduct magnetically guided photoinduced hyperthermia at first and second NIR biological windows. Adv Funct Mater. 2015; 25: 6527-37.
56. Cabrera D, Camarero J, Ortega D, Teran FJ. Influence of the aggregation, concentration, and viscosity on the nanomagnetism of iron oxide nanoparticle colloids for magnetic hyperthermia. J Nanopart Res. 2015; 17: 121.
57. Kakwere H, Leal MP, Materia ME, Curcio A, Guardia P, Niculaes D, et al. Functionalization of strongly interacting magnetic nanocubes with (thermo)responsive coating and their application in hyperthermia and heat-triggered drug delivery. ACS Appl Mater Interfaces. 2015; 7: 10132-45.
58. Zhang L, Wang H. Cuprous oxide nanoshells with geometrically tunable optical properties. ACS Nano. 2011; 5: 3257-67.
59. Pang M, Zeng HC. Highly ordered self-assemblies of submicrometer Cu_2O spheres and their hollow chalcogenide derivatives. Langmuir. 2010; 26: 5963-70.
60. Ren K, Yin P, Zhou Y, Cao X, Dong C, Cui L, et al. Localized defects on copper sulfide surface for enhanced plasmon resonance and water Splitting. Small. 2017; 13.
61. Zhao Y, Pan H, Lou Y, Qiu X, Zhu J, Burda C. Plasmonic $Cu_{2-x}S$ nanocrystals: optical and structural properties of copper-deficient copper(I) sulfides. J Am Chem Soc. 2009; 131: 4253-61.
62. Hemery G, Genevois C, Couillaud F, Lacomme S, Gontier E, Ibarboure E, et al. Monocore vs. multicore magnetic iron oxide nanoparticles: uptake by glioblastoma cells and efficiency for magnetic hyperthermia. Mol Syst Des Eng. 2017; 2: 629-39.
63. Hemery G, Keyes AC, Jr., Garaio E, Rodrigo I, Garcia JA, Plazaola F, et al. Tuning sizes, morphologies, and magnetic properties of monocore versus multicore iron oxide nanoparticles through the controlled addition of water in the polyol synthesis. Inorg Chem. 2017; 56: 8232-43.
64. Ma H, Bendix PM, Oddershede LB. Large-scale orientation dependent heating from a single irradiated gold nanorod. Nano Lett. 2012; 12: 3954-60.
65. Wang S, Riedinger A, Li H, Fu C, Liu H, Li L, et al. Plasmonic copper sulfide nanocrystals exhibiting near-infrared photothermal and photodynamic therapeutic effects. ACS Nano. 2015; 9: 1788-800.
66. Li Y, Cupo M, Guo L, Scott J, Chen YT, Yan B, et al. Enhanced reactive oxygen species through direct copper sulfide nanoparticle-doxorubicin complexation. Nanotechnology. 2017; 28: 505101
67. Kadiiska MB, Hanna PM, Hernandez L, Mason RP. In vivo evidence of hydroxyl radical formation after acute copper and ascorbic acid intake: electron spin resonance spin-trapping investigation. Mol Pharmacol. 1992; 42: 723-9.
68. Cross JB, Currier RP, Torraco DJ, Vanderberg LA, Wagner GL, Gladen PD. Killing of bacillus spores by aqueous dissolved oxygen, ascorbic acid, and copper ions. Appl. Environ Microbiol. 2003; 69: 2245-52.
69. Norouzi H, Khoshgard K, Akbarzadeh F. In vitro outlook of gold nanoparticles in photo-thermal therapy: a literature review. Lasers Med Sci. 2018; 33: 917-26.
70. Clerc P, Jeanjean P, Hallali N, Gougeon M, Pipy B, Carrey J, et al. Targeted magnetic intra-lysosomal hyperthermia produces lysosomal reactive oxygen species and causes caspase-1 dependent cell death. J Control Release. 2018; 270: 120-34.